Molecular Therapy
Nucleic Acids
Original Article

Whole-transcriptome analysis of aluminum-exposed rat hippocampus and identification of ceRNA networks to investigate neurotoxicity of Al

Chanting He,[1,2,3,4,5] Xiaoyan Zhao,[1,5] Yang Lei,[1] Jisheng Nie,[1] Xiaoting Lu,[1] Jing Song,[1] Linping Wang,[1] Huan Li,[1] Fangqu Liu,[1] Yidan Zhang,[1] and Qiao Niu[1,2,3]

[1]Department of Occupational Health, School of Public Health, Shanxi Medical University, Taiyuan, Shanxi 030001, China; [2]Key Lab of Environmental Hazard and Health of Shanxi Province, Shanxi Medical University, Taiyuan, Shanxi 030001, China; [3]Key Lab of Cellular Physiology of Education Ministry, Shanxi Medical University, Taiyuan, Shanxi 030001, China; [4]Department of Anatomy, Shanxi Medical University, Taiyuan, Shanxi 030001, China

Aluminum is a known neurotoxin that can induce Aβ deposition and abnormal phosphorylation of tau protein, leading to Alzheimer disease (AD)-like damages such as neuronal damage and decreased learning and memory functions. In this study, we constructed a rat model of subchronic aluminum maltol exposure, and the whole-transcriptome sequencing was performed on the hippocampus of the control group and the middle-dose group. A total of 167 miRNAs, 37 lncRNAs, 256 mRNAs, and 64 circRNAs expression changed. The Kyoto Encyclopedia of Genes and Genomes showed that PI3K/AKT pathway was the most enriched pathway of DEGs, and IRS1 was the core molecule in the PPI network. circRNA/lncRNA-miRNA-mRNA networks of all DEGs, DEGs in the PI3K/AKT pathway, and IRS1 were constructed by Cytoscape. Molecular experiment results showed that aluminum inhibited the IRS1/PI3K/AKT pathway and increased the content of Aβ and tau. In addition, we also constructed an AAV intervention rat model, proving that inhibition of miR-96-5p expression might resist aluminum-induced injury by upregulating expression of IRS1. In general, these results suggest that the ceRNA networks are involved in the neurotoxic process of aluminum, providing a new strategy for studying the toxicity mechanism of aluminum and finding biological targets for the prevention and treatment of AD.

INTRODUCTION

Aluminum (Al) is the most abundant metal element in nature. Because of its excellent properties, aluminum is widely used in transportation, construction, cooking utensils, vaccine adjuvants, and food additives.[1] Aluminum ultrafine particles or ions enter the human body through the respiratory system, digestive system, skin, etc., and the body's aluminum load increases, making aluminum exposure a public health issue that people are increasingly concerned about.[2] During occupational exposure, the bioavailability of inhaled aluminum ultrafine particles is high, so aluminum exposure is also a serious occupational health problem.[3]

With the wide application of metallic aluminum, there are more and more studies on the toxicity of aluminum. Many scholars believe that aluminum is one of the most important environmental factors for neurodegenerative diseases, especially Alzheimer disease (AD).[4] Cohort studies have shown that the incidence of AD in the elderly increases significantly after long-term drinking of water with excessive aluminum.[5] Animal experiments have also confirmed that acute aluminum exposure can cause damage to the nervous system, while long-term chronic aluminum exposure can cause cognitive impairment and decline in learning and memory, and it has a significant relationship with the exposure dose.[6,7] Riihimäki et al. reported that the cognitive ability of aluminum workers decreased, and it became more serious as the internal exposure level increased.[8]

The neurotoxicity mechanism of aluminum has been studied from different directions. Aluminum can inhibit acetylcholinesterase, thereby affecting the conduction of nerve impulses.[9] Aluminum can damage mitochondrial membranes, increase reactive oxygen species, produce oxidative stress, and can cause nerve cell apoptosis and programmed necrosis.[10,11] Animal models of oral intake of aluminum showed significant accumulation of Aβ and accelerated aggregation of tau protein.[12,13] We also found that aluminum reduces the learning and memory function of rats by impairing the synaptic plasticity of the hippocampus.[14] But which pathways are involved in the neurotoxicity mechanism of aluminum remain to be discovered.

Transcriptome sequencing includes mRNA sequencing, noncoding RNA sequencing, and other RNA sequencing (RNA-seq). Through sequencing and analysis, the overall transcription activity of any species can be evaluated, and new transcripts, fusion genes, and alternative splicing points can be identified.[15] Therefore, transcriptome

Received 12 April 2021; accepted 4 November 2021;
https://doi.org/10.1016/j.omtn.2021.11.010.

[5]These authors contributed equally

Correspondence: Qiao Niu, PhD, Department of Occupational Health, School of Public Health, Shanxi Medical University, Taiyuan, Shanxi 030001, China.
E-mail: niuqiao55@163.com

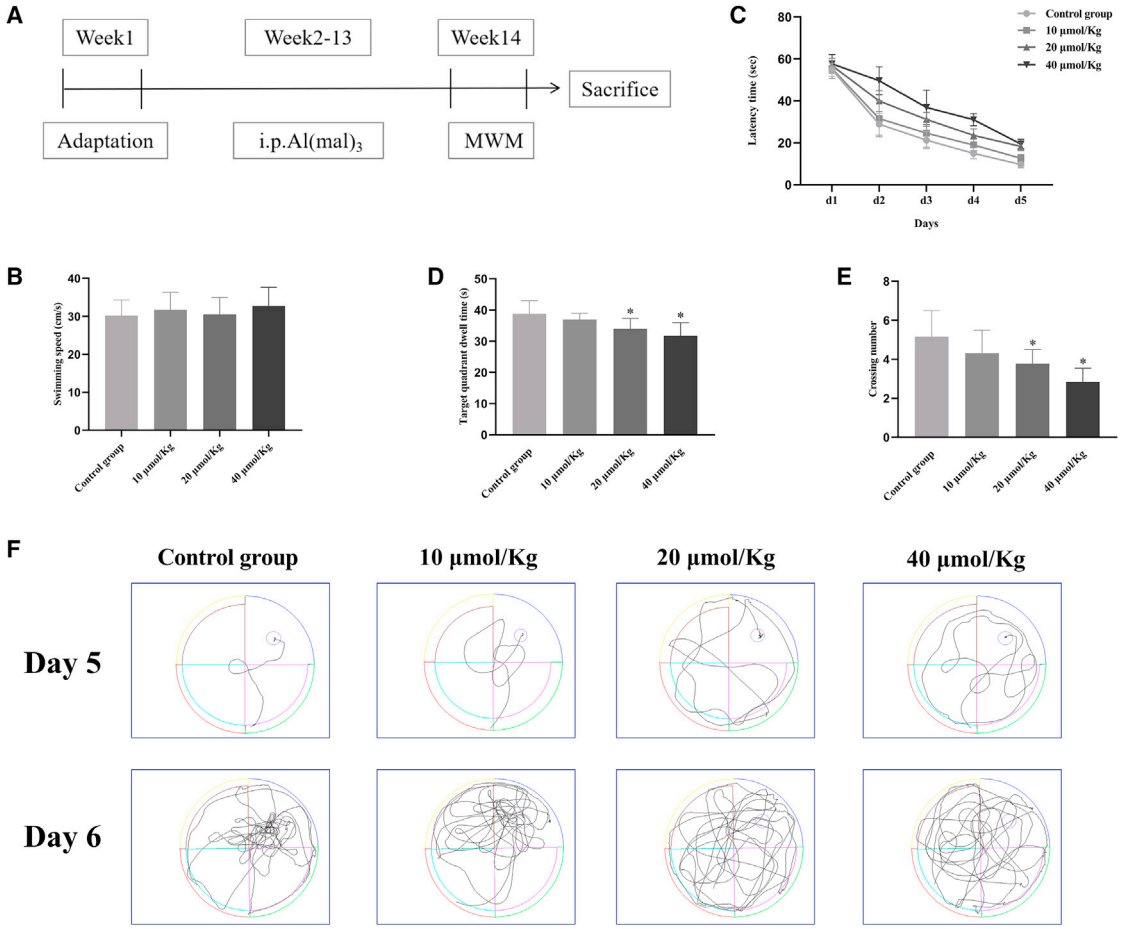

Figure 1. MWM results of control, 10, 20, and 40 μmol/kg Al(mal)$_3$ groups

(A) Experimental design: construction of a rat model of aluminum exposure. (B) Swimming speed of rats in each group. (C) The escape latency period in the positioning navigation experiment. (D) The target quadrant dwell time in the space exploration experiment. (E) The number of rats crossing the platform in the space exploration experiment. (F) Representative swimming trajectory in each group on the fifth and sixth day. Compared with the control group, *$p < 0.05$. N = 13.

sequencing is a popular method for studying tumors, immune diseases, and neurological diseases in recent years.[16–18] Researchers have used transcriptomics analysis to study the mechanism of metal toxins such as lead, mercury, and cadmium, so it can also be used to explore the toxicity mechanism of aluminum.[19–21] As we all know, mRNA is transcribed from DNA and carries genetic information. MicroRNA (miRNA) will degrade target mRNA or inhibit its translation, and play a post-transcriptional regulatory role, thereby negatively regulating gene expression.[22] The competing endogenous RNA (ceRNA) regulates gene expression by competitively binding miRNA.[23] The ceRNA network composed of long noncoding RNA (lncRNA)/circular RNA (circRNA)-miRNA-mRNA has attracted attention.[24,25]

In this study, we constructed an aluminum maltol (Al(mal)$_3$) exposed rat model and performed hippocampal whole-transcriptome sequencing to discover different expressed mRNAs, miRNAs, circRNAs, and lncRNAs, and identify the signaling pathways involved in the aluminum toxicity mechanism and construct ceRNA networks of core pathways and core molecules. The results were preliminarily verified by reverse-transcriptase quantitative polymerase chain reaction (RT-PCR), western blotting, enzyme linked immunosorbent assay (ELISA), immunohistochemistry (IHC), and other experiments. In addition, we constructed an adeno-associated virus (AAV) intervention rat model to further verify the authenticity of the ceRNA network and reveal the possible mechanism of aluminum neurotoxicity.

RESULTS

Aluminum impaired learning and memory ability of rats

Figure 1A showed the schematic diagram of a rat model of subchronic aluminum exposure. In this experiment, there was no statistical difference in the swimming speed of the rats in each group (Figure 1B), indicating that the aluminum exposure did not damage the exercise ability of the rats. The positioning navigation experiment showed that with the extension of training time, the escape

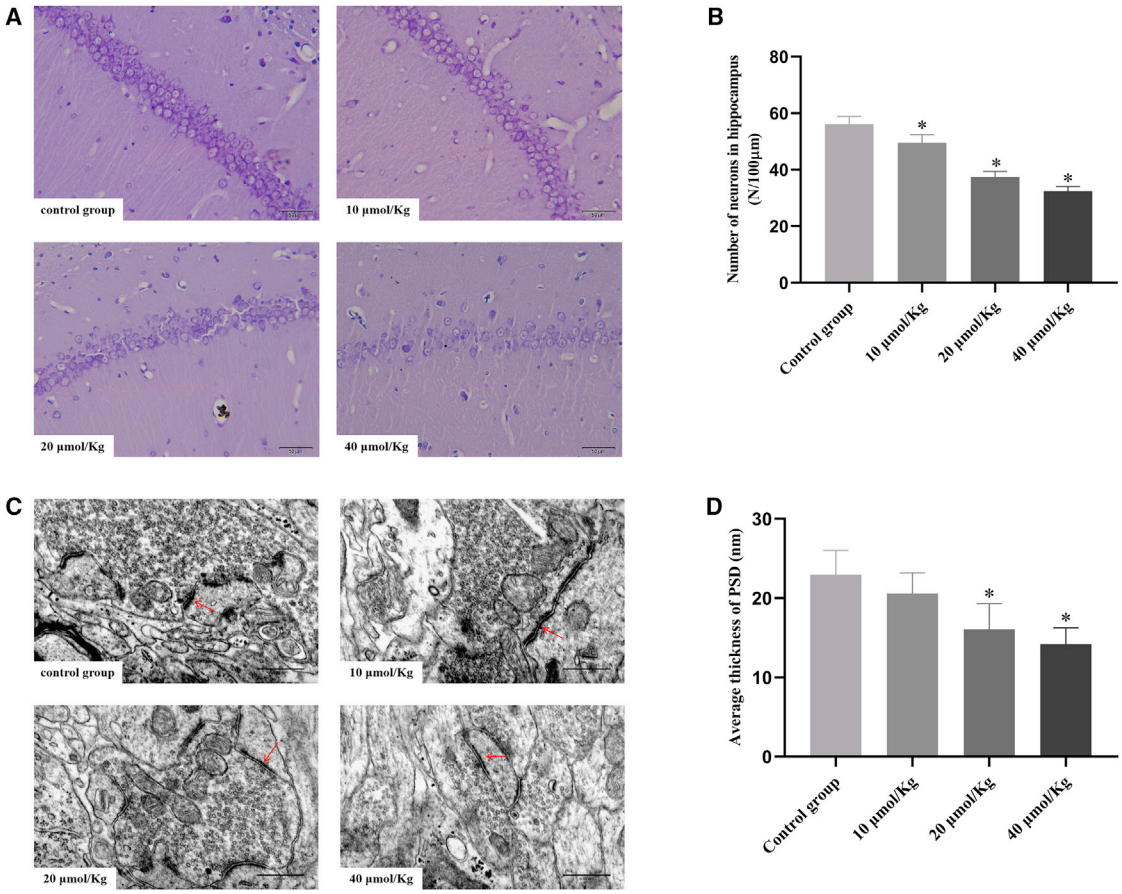

Figure 2. Effects of Al(mal)$_3$ on neurons and synaptic structure

(A) The results of Nissl staining in hippocampal CA1 region of rats in control, 10-, 20-, and 40-μmol/kg Al(mal)$_3$ groups. Magnification ×400. (B) Quantification of the number of neurons. N = 3. (C) The results of TEM in hippocampal CA1 region of rats in control, 10-, 20-, and 40-μmol/kg Al(mal)$_3$ groups. Magnification ×60,000.The red arrow: synaptic structure. (D) Quantification of the average thickness of PSD. N = 3. Compared with the control group, *p < 0.05.

latency of rats gradually shortened in each group (Figure 1C). The daily escape latency period was analyzed by one-way ANOVA. The results showed that there was no statistical difference in the escape latency period between different aluminum-exposure groups on the first day (F = 1.275, p = 0.294). Compared with the control group on the same day, the escape latency period of rats in the 20 μmol/kg and 40 μmol/kg groups was prolonged on days 2 to 5, and the difference was statistically significant (p < 0.05). As shown in Figures 1D and 1E, in the space exploration experiment on the sixth day, as the aluminum exposure dose increased, the target quadrant dwell time of rats gradually shortened (F = 9.656, p < 0.05), and the number of crossing the platform gradually decreased (F = 11.579, p < 0.05), and the difference was statistically significant. Figure 1F shows the swimming trajectory. With the increase of training days, the swimming trajectory of the rats in the control group became clearer and clearer and reached the platform purposefully. Although the rats in the aluminum-exposed group could finally reach the platform, their swimming trajectories were chaotic and random. The results of the water maze suggested that subchronic aluminum exposure could damage the learning and memory function of rats in a dose-dependent manner.

Aluminum damaged neurons and synaptic structure of hippocampus CA1 in rats

In order to assess the effects of aluminum exposure on hippocampus, Nissl staining was used to count neurons to see if any neurons were lost. As can be seen from Figure 2A, the neurons in the CA1 area of the hippocampus in the control group were in complete morphology, a large number, and tightly arranged, with Nissl bodies clearly visible. With the increase of the aluminum-exposure dose, the number of neurons was significantly reduced, and the arrangement was loose. Compared with the control group, the difference was statistically significant (p < 0.05) (Figure 2B).

Transmission electron microscopy (TEM) can see fine structures smaller than 0.2 μm, such as the synaptic structure shown by the red arrow in Figure 2C. The synapse morphology of the hippocampal neurons in the control group was good, the presynaptic membrane

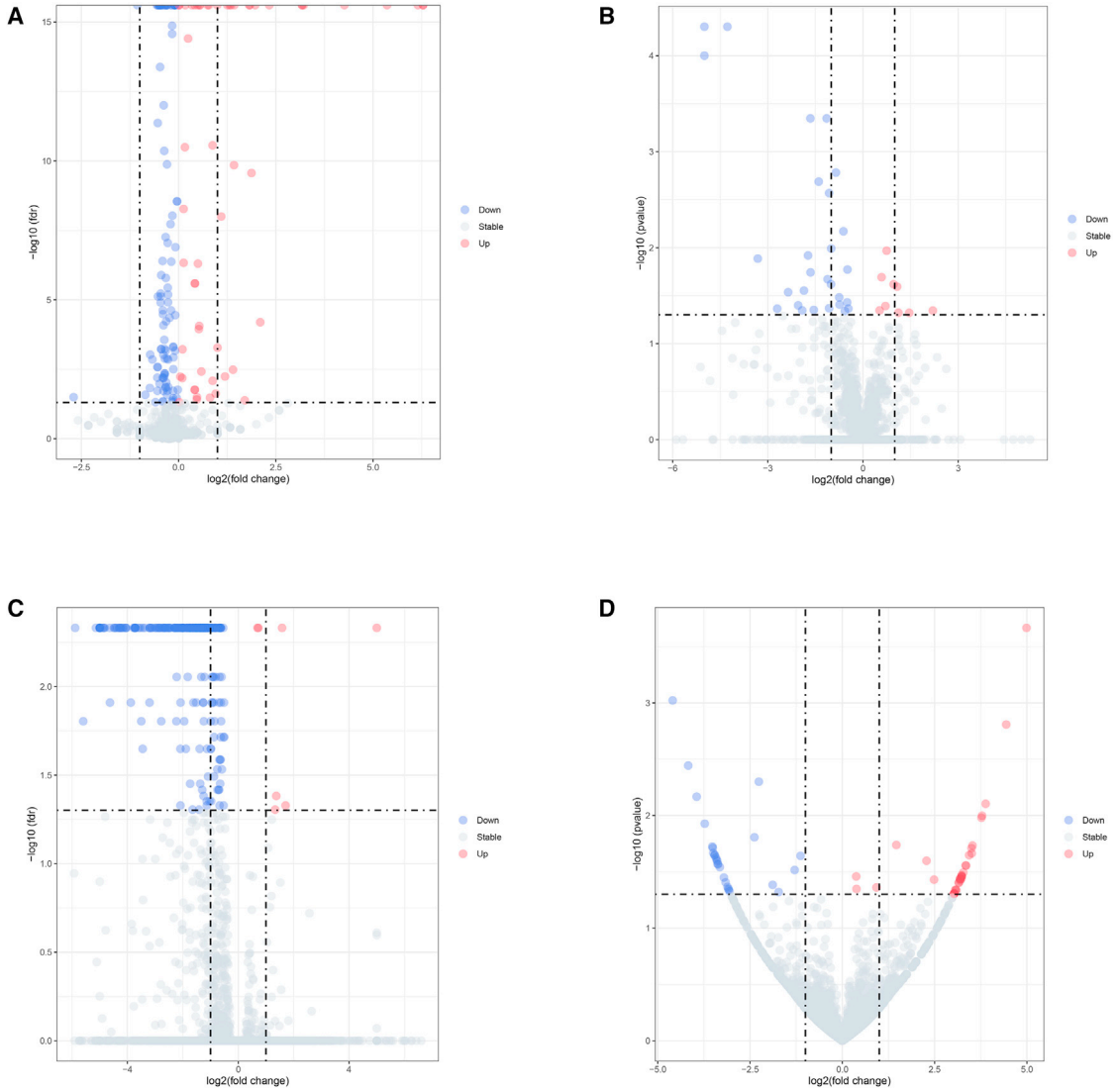

Figure 3. Differential expression of miRNA, lncRNA, mRNA, and circRNA in hippocampus after aluminum exposure

(A) Volcano plot of DE-miRNAs. (B) Volcano plot of DE-lncRNAs. (C) Volcano plot of DE-mRNAs. (D) Volcano plot of DE-circRNAs. The red dots represent transcripts that were up-regulated in the aluminum-exposed group compared with the control group. The blue dots represent the down-regulated transcripts.

was rich in synaptic vesicles, and the post-synaptic dense area was thicker, indicating that it has good synaptic function. With the increase of aluminum exposure, the synaptic structure of hippocampal CA1 neurons changed, and the post-synaptic compact area became thinner (Figure 2D), so synaptic function may be affected accordingly. Therefore, subchronic aluminum exposure may damage the synaptic plasticity of neurons in the CA1 region of the hippocampus of rats.

Overview of miRNA, lncRNA, mRNA, and circRNA sequencing data

Each sample contained 13M high-quality reads (12–15M), with Q30 bases accounting for more than 95%. We filtered these results based on length (18–35 nt), and it showed that each sample retained 10M reads (8–12M). The selected reads were compared with the rat reference sequence, and the average comparison rate of each sample was over 99%. An average of 6.4M known miRNAs (5.4–8.4M) were detected per sample. An average of 15k novel miRNAs (5–25k) were identified per sample. The result showed that there were 167 DE-miRNA transcripts in Al-exposed rats compared with controls, including 60 that were up-regulated and 107 that were down-regulated (Figure 3A). All DE-miRNAs are listed in Table S1.

A library was constructed using lncRNA and mRNA. Each sample contained 92M high-quality reads (83–102M), and Q30 bases accounted for more than 91%. These reads were compared with the

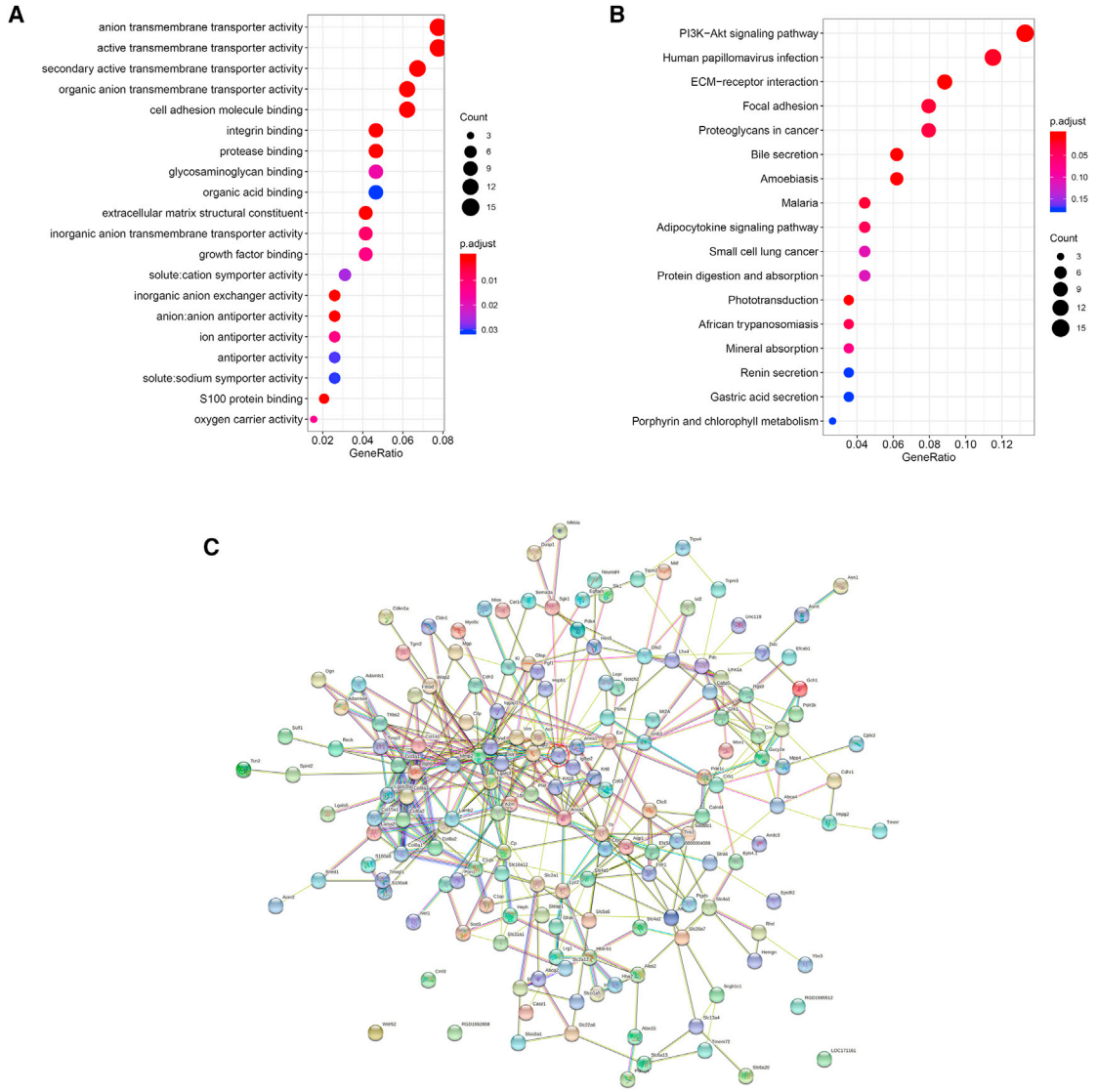

Figure 4. GO terms, KEGG enriched pathways and PPI network of DEGs

(A) GO analysis of all the DEGs between control group and aluminum-exposed group. (B) Statistics of pathways enrichment of all the DEGs between control group and aluminum-exposed group. (C) PPI diagram. The red circle is IRS1.

reference genome, and the average comparison rate of each sample was over 87%. A total of 37 DE-lncRNAs were obtained in Al-exposed group compared with the control group, including nine up-regulated and 28 down-regulated (Figure 3B); 256 differentially expressed genes (DEGs), including seven up-regulated and 249 down-regulated in Al-exposed rats, were identified (Figure 3C). All DE-lncRNAs and DEGs are listed in Tables S2 and S3.

For circRNA, each sample contained 92M high-quality reads (82–102M), and the percentage of Q30 bases was more than 92%. On average, 471 known cirRNAs (405–516) and 2,400 novel cirRNAs (2084–2600) were detected in each sample. Thirty-seven up-regulated and 27 down-regulated circRNAs were identified in Al-exposed rats compared with controls (Figure 3D). All DE-circRNAs are listed in Table S4.

Gene ontology annotations, Kyoto Encyclopedia of Genes and Genomes pathway analysis, and protein-protein interaction network

Gene ontology (GO) analysis was implemented on the DEGs and several GO terms were found to be significantly enriched (Figure 4A): anion transmembrane transporter activity (GO:0008509), active transmembrane transporter activity (GO:0022804), cell adhesion molecule binding (GO:0050839), integrin binding (GO:0005178),

Table 1. DEGs in PI3K/AKT pathway of Al-treated rats compared to control

	Gene_name	Al-treated group (FPKM)	Control group (FPKM)	log2 (foldchange)	p value	Gene description
1	Irs1	6.45276	10.3633	−0.68349	0.00005	insulin receptor substrate 1
2	Gnb3	0.645884	19.8584	−4.94233	0.00005	G protein subunit beta 3
3	Vwf	6.46679	21.271	−1.71777	0.00005	von Willebrand factor
4	Itgb6	0.160207	1.46191	−3.18984	0.00005	integrin subunit beta 6
5	Fn1	3.78279	9.79902	−1.37319	0.00005	fibronectin 1
6	Col6a2	3.20574	5.8765	−0.8743	0.00005	collagen type VI alpha 2 chain
7	Sgk1	44.7435	115.641	−1.3699	0.00005	serum/glucocorticoid regulated kinase 1
8	Fgf1	0.914646	3.67473	−2.00635	0.00005	fibroblast growth factor 1
9	Cdkn1a	5.23479	11.5729	−1.14455	0.00005	cyclin dependent kinase inhibitor 1A
10	Thbs2	0.88797	2.62285	−1.56255	0.00005	thrombospondin 2
11	Lama2	1.74869	3.9672	−1.18184	0.00005	laminin subunit alpha 2
12	Igf2	7.55965	48.7827	−2.68998	0.00005	insulin-like growth factor 2
13	Col9a3	5.089	9.22543	−0.858233	0.0002	collagen type IX alpha 3 chain
14	Col1a1	1.49169	2.73112	−0.872545	0.00025	collagen type I alpha 1 chain
15	Lamb2	7.48994	10.8247	−0.531298	0.0007	laminin subunit beta 2

and protease binding (GO:0002020). Kyoto Encyclopedia of Genes and Genomes (KEGG) pathway analysis was performed to confirm the signaling cascades related to the DEGs. Based on the thresholds of $p < 0.05$, we identified the following significantly enriched pathways (Figure 4B): PI3K/AKT signaling pathway (rno04151), human papillomavirus infection (rno05165), ECM-receptor interaction (rno04512), focal adhesion (rno04510), proteoglycans in cancer (rno05205), bile secretion (rno04976), and amebiasis (rno05146). Our results showed that major genes were enriched in PI3K/AKT signaling pathway and previous research proved that PI3K/AKT pathway weakened in the brain of AD patients.[26] Table 1 shows the DEGs on the PI3K/AKT signaling pathway in the Al-exposed group. All the meaningful GO annotations and KEGG pathways are listed in Tables S5 and S6.

String was performed to explore the protein-protein interaction (PPI) of 256 co-expressed DEGs (Figure 4C). IRS1 is at the core position, and it interacts with SGK1, PDK4, KI, LEPR, POMC, ACE, IGF2, TNS1, and other proteins.

The ceRNA networks of all the DEGs

According to the ceRNA hypothesis, circRNA and lncRNA can serve as ceRNA to compete for miRNA response elements, thus regulating the expression level of target genes. We developed circRNA and lncRNA-associated ceRNA networks with Cytoscape. Both ceRNA networks could be divided into up- and down-regulated networks according to the DEGs expression. These two networks were parachute type, and the lowest molecule of the parachute may be the core molecule (skydiver) in the whole network. In the circRNA-associated ceRNA network, rno-miR-101b-3p was the skydiver in the up-regulated network and rno-miR-665 in the down-regulated ceRNA network (Figures 5A and S7). It showed the same result in the lncRNA-associated ceRNA network (Figures 5B and S8). Rno-miR-101b-3p was lowly expressed in Al-exposed group, and its related genes, circRNAs and lncRNAs were highly expressed, including glial fibrillary acidic protein (GFAP), rno_circ_0004500, rno_circ_0007293, rno_circ_0008086, LNC_001074, LNC_000346, and so on. Rno-miR-665 was highly expressed in Al-exposed group, and its related genes, circRNAs, and lncRNAs were lowly expressed, including IGF2, VWF, GNB3, Col1a1, rno_circ_0001722, rno_circ_0005551, rno_circ_0008322, rno_circ_0006872, LNC_000772, LNC_001209, LNC_001398 and so on.

The ceRNA networks of DEGs in PI3K/AKT signaling pathway

We constructed circRNA-miRNA-target gene network and lncRNA-miRNA-target gene network with DEGs in PI3K/AKT pathway using Cytoscape. In the circRNA network, rno_circ_0001722 played its central role, which could regulate the expression of corresponding genes through multiple miRNAs, thus participating in the neurotoxic process of aluminum (Figure 5C). However, rno-miR-34c-5p was a central molecule in the lncRNA network in PI3K pathway (Figure 5D).

The ceRNA networks of insulin receptor substrate 1

Insulin receptor substrate 1 (IRS1) is the upstream molecule of PI3K pathway, which plays an important role in the development of AD.[27] The circRNA-miRNA-IRS1 network and lncRNA-miRNA-IRS1 network were constructed separately. Multiple circRNAs were predicted to regulate the expression of IRS1 by functioning as sponges of rno-miR-96-5p, rno-miR-143-5p, rno-miR-144-3p, rno-miR-145-5p, rno-miR-183-5p and rno-miR-337-3p (Figure 5E). Rno-miR-143-5p located in the middle of the circle, and ceRNA networks such as rno_circ_0001722/rno_circ_0005888/rno_circ_0006529- rno-miR-143-5p- IRS1 are involved in regulating the expression of IRS1. Accordingly, multiple lncRNAs were predicted to regulate the expression of

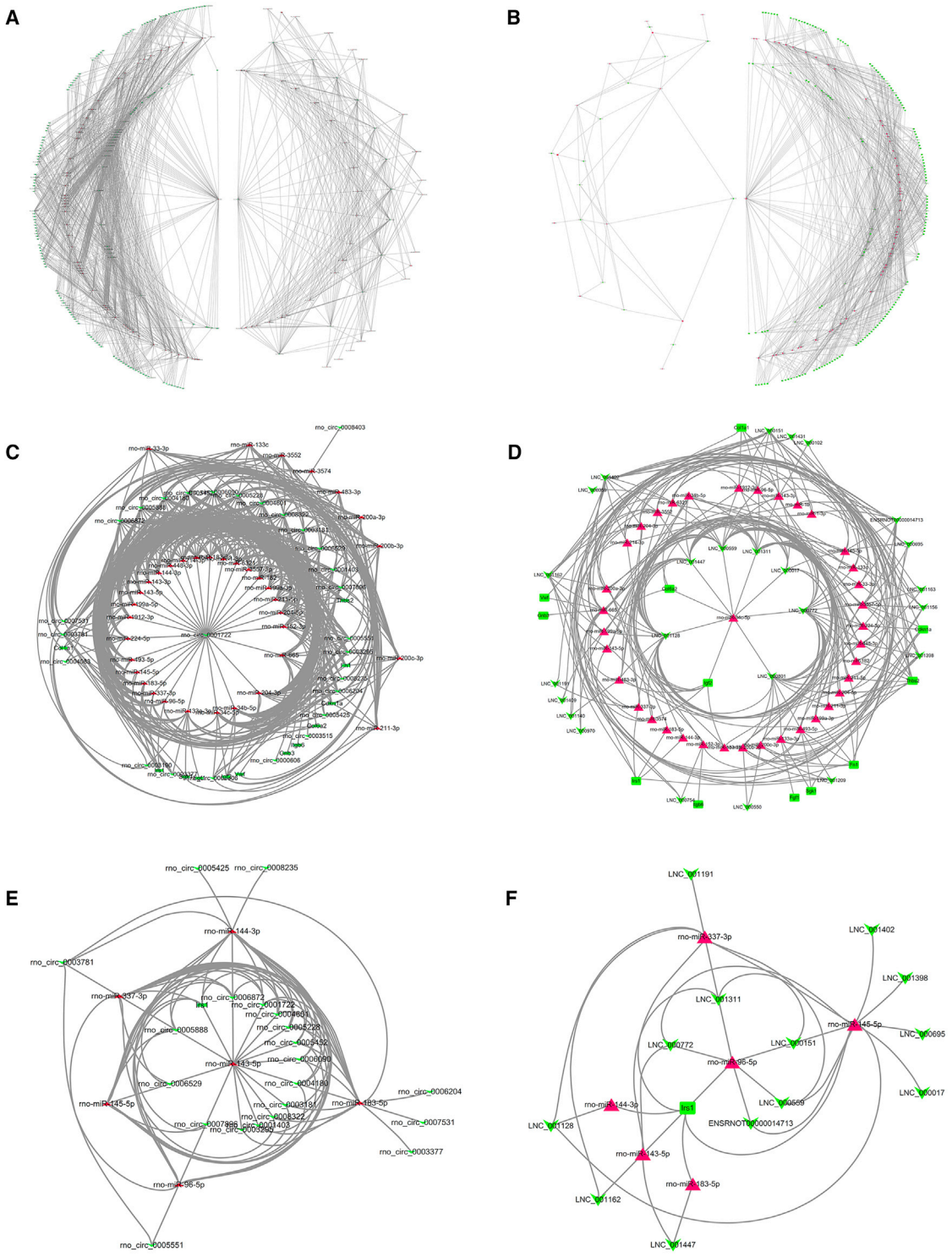

Figure 5. The ceRNA networks

(A) circRNA-miRNA-mRNA network of all the DEGs. (B) lncRNA-miRNA-mRNA network of all the DEGs. (C) circRNA-miRNA-mRNA network of DEGs in PI3K/AKT pathway. (D) lncRNA-miRNA-mRNA network of DEGs in PI3K/AKT pathway. (E) circRNA-miRNA-IRS1 network. (F) lncRNA-miRNA-IRS1 network.

IRS1 by functioning as sponges of the same miRNAs (Figure 5F). Rno-miR-96-5p showed its central role, and ceRNA networks such as LNC_000151/LNC_000559/LNC_000772/LNC_001311- rno-miR-96-5p- IRS1 are involved in regulating the expression of IRS1.

RT-PCR validation

To confirm the accuracy of identifying differential expression results in our RNA-seq experiment, RT-PCR was used to analyze 10 DEGs on PI3K/AKT pathway and several IRS1-related miRNA, circRNA, and lncRNA expressions. All selected transcripts were detected in the hippocampus of control group rats and 20 μmol/kg $Al(mal)_3$ group rats, and the PT-PCR results showed that our RNA-seq results are credible (Figure 6A).

Aluminum inhibits the IRS1/PI3K/AKT pathway, leading to $A\beta_{1-42}$ deposition and abnormal phosphorylation of Tau protein

KEGG results showed that DEGs were enriched in the PI3K/AKT pathway, and the expression of IRS1 in the aluminum-exposure group changed significantly. Therefore, western blotting was used to detect the protein changes in the IRS1/PI3K/AKT pathway in the rat hippocampus. Figures 6C and 6D showed that with the increase of aluminum-exposure dose, the expression of IRS1 decreased, and there were statistical differences in 20 and 40 μmol/kg $Al(mal)_3$ groups compared with the control group. The expression levels of AKT and p-AKT (Ser473) also showed the same trend. The total protein expression level of GSK3β, a downstream protein of this pathway, did not change, but p-GSK3β (Ser9) was significantly reduced, which is related to Aβ deposition and abnormal phosphorylation of tau protein. The protein levels of tau and p-tau (Ser396) increased with the increase of $Al(mal)_3$ concentration, and were positively correlated with the dose.

ELISA and IHC were performed to evaluate the effect of aluminum on $A\beta_{1-42}$ deposition in the hippocampus of rats. Both ELISA (Figure 6B) and IHC (Figures 6E and 6F) results showed that compared with the control group, there was no significant difference in the $A\beta_{1-42}$ content of the 10 μmol/kg group ($p > 0.05$), while the $A\beta_{1-42}$ levels of the 20 and 40 μmol/kg groups were increased significantly ($p < 0.05$), indicating that aluminum exposure would lead to the deposition of $A\beta_{1-42}$ in the hippocampus, thereby affecting the learning and memory ability of rats.

Inhibition of miR-96-5p resists aluminum-induced impairment of learning and memory

The ceRNA results showed that the expression of miR-96-5p increased after aluminum exposure and could regulate the expression of IRS1. To continue this research, AAV-miR-96-5p-sponge virus was injected into the hippocampus of rats to test whether it is involved in regulating the neurotoxic effects of aluminum (Figures 7A and 7B). A large amount of GFP in the neurons in the CA1 region of the rat hippocampus could be seen in the frozen section, indicating that AAV has successfully infected the hippocampal neuronal cells (Figure 7C).

The water maze results showed that there was no difference in the swimming speed of the rats in each group, indicating that brain surgery and aluminum exposure did not damage the exercise ability of the rats (Figure 7D). The escape latency of rats in each group gradually shortened with the increase of training days, and there was no difference between control group and AAV-control group, $Al(mal)_3$ group, and $Al(mal)_3$+AAV-control group ($p > 0.05$), which ruled out the influence of AAV virus vector on rats (Figure 7E). The escape latency of $Al(mal)_3$+AAV-miR-96-5p-sponge group was significantly lower than that of $Al(mal)_3$ group on days 2 to 5 ($p < 0.05$), indicating that inhibition of miR-96-5p could improve learning and memory impairment caused by $Al(mal)_3$. Compared with the control group, the target quadrant dwell time and the number of crossing the platform in the $Al(mal)_3$ group and $Al(mal)_3$+AAV-control group were significantly reduced ($p < 0.05$) (Figures 7F and 7G). However, compared with the $Al(mal)_3$ group, the results of the $Al(mal)_3$+AAV-miR-96-5p-sponge group were significantly higher ($p < 0.05$). These results indicated that inhibiting the expression of hippocampal miR-96-5p could reverse the impairment of learning and memory in rats caused by aluminum exposure.

miR-96-5p regulates the neurotoxic effects of aluminum through the IRS1/PI3K/AKT pathway

The morphology observation showed the same results as the behavior experiment. Compared with the control group, the number of neurons and the thickness of post-synaptic density (PSD) in the hippocampal CA1 of the $Al(mal)_3$ group and the $Al(mal)_3$+AAV-control group were significantly reduced ($p < 0.05$) (Figures 8A–8D). However, compared with the $Al(mal)_3$ group, these results of the $Al(mal)_3$+AAV-miR-96-5p-sponge group were significantly higher ($p < 0.05$). These results suggested that the low expression of miR-96-5p could ameliorate the number loss and structural impairment of neurons in rats caused by aluminum exposure.

ceRNA results showed that miR-96-5p targets the expression of IRS1, and PCR results verified this correlation (Figure 8E). Aluminum reduced the mRNA level of IRS1, and inhibition of miR-96-5p could reverse this change. ELISA experiment showed that compared with the control group, the $A\beta_{1-42}$ content of the $Al(mal)_3$ group and the $Al(mal)_3$+AAV-control group were significantly increased ($p < 0.05$), but the $Al(mal)_3$+AAV-miR-96-5p-sponge group reverse this change (Figure 8F). The $A\beta_{1-42}$ content in the AAV-miR-96-5p-sponge group was lower than that in the control group ($p < 0.05$), indicating that miR-96-5p was involved in the $A\beta_{1-42}$ deposition process. Western blotting results showed that aluminum inhibited the IRS1/PI3K/AKT pathway, resulting in abnormal phosphorylation of tau protein (Figures 8G and 8H). The injection of AAV-miR-96-5p-sponge into the CA1 region activated the IRS1/PI3K/AKT pathway, reduced the expression of tau protein, and reversed the neurotoxicity caused by aluminum.

DISCUSSION

Aluminum is the third most abundant element on the earth, second only to oxygen and silicon. After the method of electrolyzing

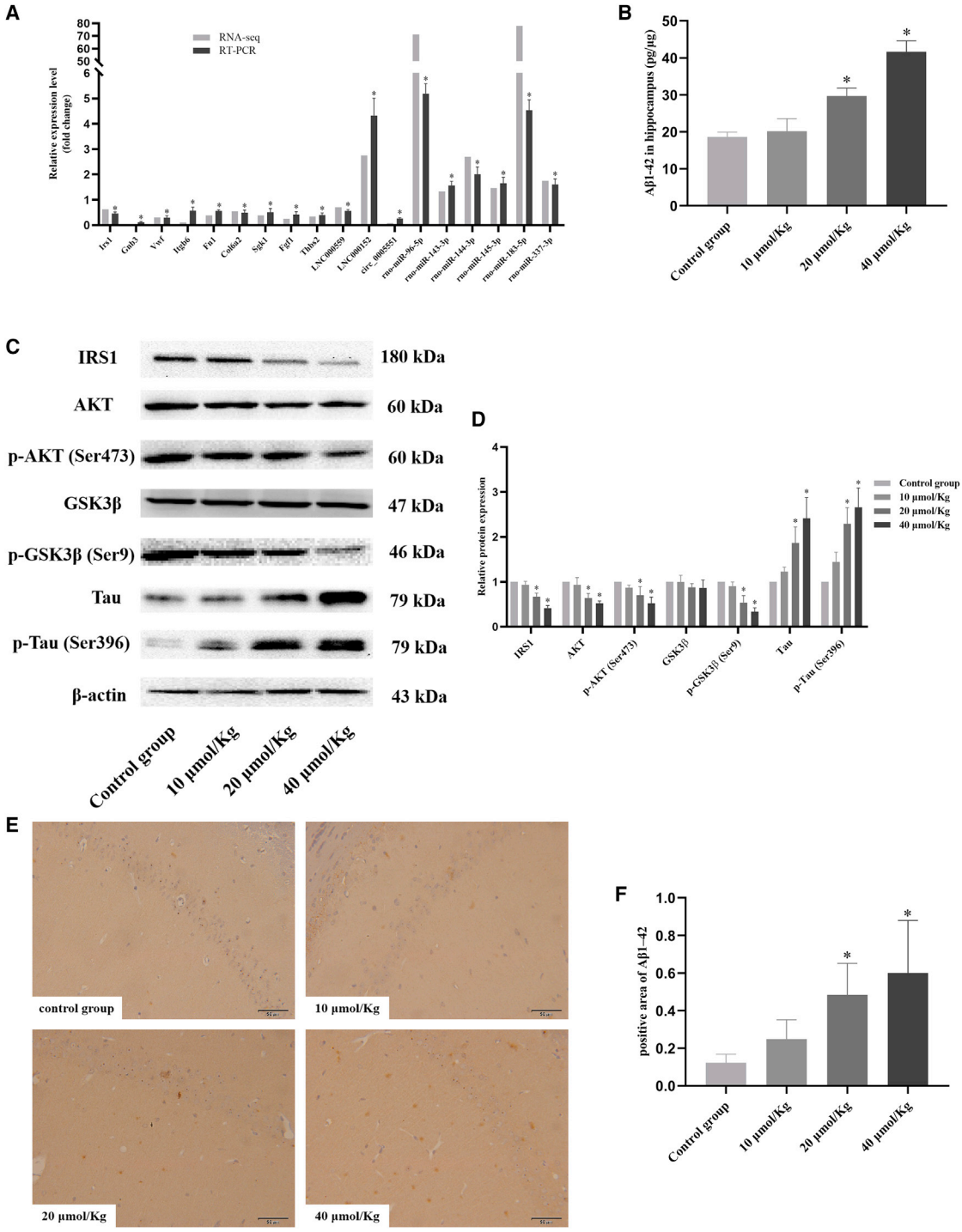

Figure 6. Laboratory verification results

(A) RT-PCR validation of RNA-seq for differentially expressed transcripts. N = 6. (B) The changes of $A\beta_{1-42}$ content in rat hippocampus were measured by ELISA. N = 4. (C) Changes in protein expression of PI3K/AKT pathway after aluminum exposure. (D) Protein expression statistics graph. N = 4. (E) Expression distribution of $A\beta_{1-42}$ in hippocampal CA1 area. (F) The percentage of $A\beta_{1-42}$ positive area in the CA1 area of the hippocampus. N = 3. Compared with the control group, *$p < 0.05$.

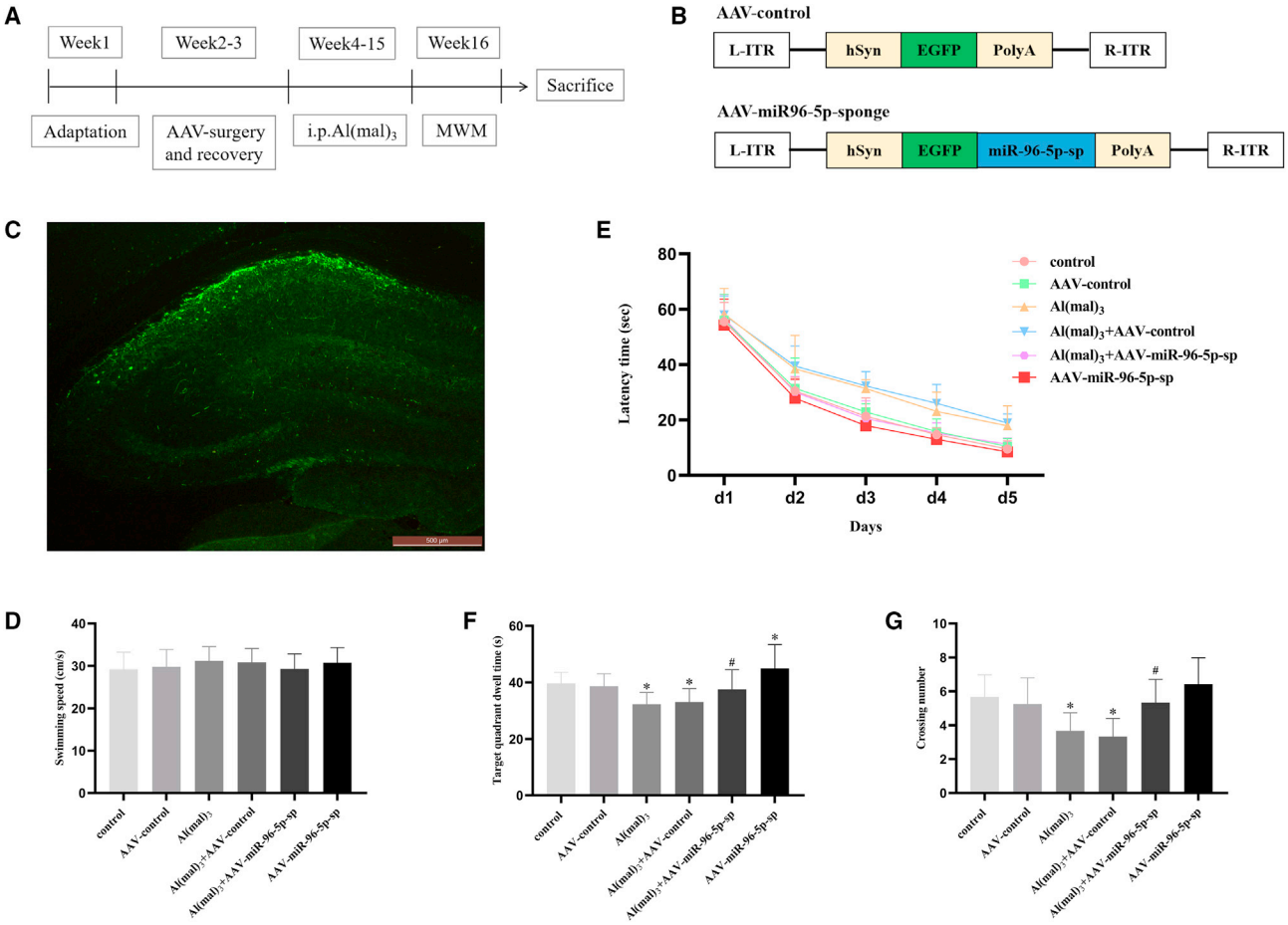

Figure 7. Effect of miR-96-5p on learning and memory impairment in rats induced by aluminum

(A) Experimental design: construction of a rat model of AAV intervention. (B) Schematic diagram of AAV vector. (C) Representative fluorescence image of rat hippocampus after the establishment of the AAV intervention model. Magnification ×40. (D) Swimming speed of rats in each group. (E) The escape latency period in the positioning navigation experiment. (F) The target quadrant dwell time in the space exploration experiment. (G) The number of rats crossing the platform in the space exploration experiment. Compared with the control group, *$p < 0.05$. Compared with the $Al(mal)_3$ group, $^{\#}p < 0.05$. N = 10.

aluminum was improved in 1886, the price of aluminum dropped. With its lightness, corrosion resistance, and other characteristics, aluminum was widely used in drinking water treatment systems, cosmetics, and vaccine adjuvants.[28] Exley and Mold reported that aluminum does not have any known biological effects in the human body, and the biological processes in existing biota do not require aluminum.[29] As early as 1973, Crapper et al. found that in higher mammals, aluminum can degenerate their neurons, and in some brain regions of AD patients, aluminum was found to be close to the experimental concentration.[30] Since then, more and more evidence has shown that aluminum is an important factor in the development of AD.[31]

The main clinical manifestation of AD patients is progressive cognitive decline. In the survey of occupational aluminum exposure, Giorgianni et al. found that aluminum workers also showed memory loss, and decreased reaction speed and abstract reasoning ability.[32] The characteristic pathological changes of AD patients include Aβ deposition to form senile plaques and abnormal phosphorylation of tau protein to destroy the microtubule structure. House et al. proved that aluminum can induce the accumulation of Aβ in the rat brain.[33] Zhao et al. found that aluminum can induce abnormal phosphorylation of tau protein and make it aggregate to form neurofibrillary tangles (NFTs).[34] We have confirmed that aluminum can impair the structure and function of synaptic plasticity in rats, and reduce the expression of synaptic plasticity-related proteins in PC12 cells.[35,36] Maltol is a byproduct of sucrose hydrolysis and a safe and reliable food additive.[37] At the same time, it is also a metal ion chelating agent widely used in medicine and cosmetics.[38,39] $Al(mal)_3$ can release a large amount of aluminum ions under normal physiological pH conditions and has a high bioavailability, so it is suitable for aluminum neurotoxicity research.[40] Therefore, this study constructed a rat model of subchronic intraperitoneal injection of $Al(mal)_3$ to explore the neurotoxic effects of aluminum.

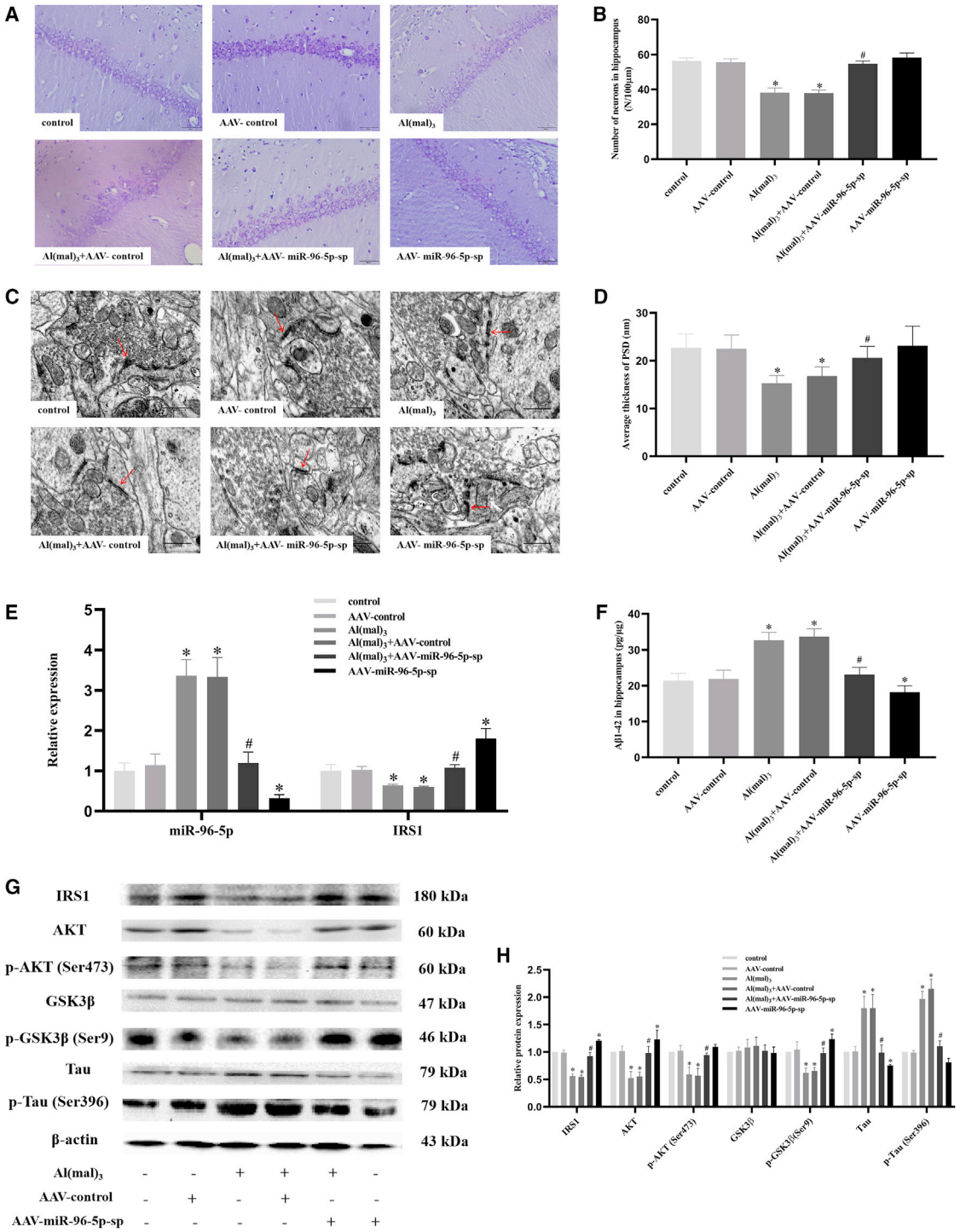

Figure 8. Blocking of miR-96-5p reduced the neurotoxicity of aluminum through the IRS1/PI3K/AKT pathway

(A) The results of Nissl staining in hippocampal CA1 region. Magnification ×400. (B) Quantification of the number of neurons. N = 3. (C) The results of TEM in hippocampal CA1 region. Magnification ×60,000. The red arrow: synaptic structure. (D) Quantification of the average thickness of PSD. N = 3. (E) Detection of miR-96-5p and IRS1 mRNA level in AAV intervention model. N = 4. (F) The changes of $A\beta_{1-42}$ content in rat hippocampus were measured by ELISA. N = 4. (G) Changes in protein expression of IRS1/PI3K/AKT pathway in AAV intervention model. (H) Protein expression statistics graph. N = 4. Compared with the control group, $^{*}p < 0.05$. Compared with the $Al(mal)_3$ group, $^{\#}p < 0.05$.

The Morris water maze is a kind of behavioral research widely used in the field of neuroscience to evaluate the learning and memory function of rodents.[41] In this study, as the concentration of $Al(mal)_3$ increased, the escape latency period of rats was prolonged, the target quadrant dwell time was shortened, and the number of crossing platforms decreased, especially in the 20 and 40 μmol/kg $Al(mal)_3$ groups of rats. The results of the Morris water maze indicated that subchronic aluminum exposure caused impairment of learning and memory in rats, and showed a certain dose-dependent effect. Nissl staining is the staining of Nissl bodies in neuron cell bodies. It is generally used to count neurons and observe whether there is neuron loss.[42] Our results showed that aluminum could reduce the number of neurons in the hippocampus, which has been manifested from 10 μmol/kg $Al(mal)_3$ group. TEM results also showed that aluminum exposure damaged the synaptic plasticity of neurons in the CA1 region of the rat hippocampus. Therefore, the results of behavioral and morphological experiments confirmed that we successfully established a rat model of subchronic aluminum exposure damaging learning and memory abilities and hippocampal neurons.

Today's RNA-seq can study RNA biology from multiple perspectives such as single-cell gene expression, structure, and translation, but differential expression is still its main application.[43] RNA-seq is widely used in toxicological analysis, and many DEGs and ncRNAs have been discovered. Li et al. found through RNA sequencing that the differential expression of egfr and cyp2c55 may be involved in the mechanism of liver injury induced by sulfasalazine (SASP).[44] Chen et al. sequenced the RNA extracted from peripheral blood mononuclear cells of 29 Bangladeshi women, and found that DAPK1, Egr2, APP, miR-155, miR-338, miR-210, and NOTCH signaling pathways play a role in the carcinogenicity of arsenic.[45] High-throughput RNA sequencing results showed that lncRpa and circRar1 increased the expression of caspase8 and p38 by regulating miR-671 to promote neuronal apoptosis, providing a new basis for the study of lead neurotoxicity mechanisms.[46] In this study, we performed RNA-seq on the hippocampus of rats in the control group and the 20 μmol/kg $Al(mal)_3$ group. The results showed that the expression of 167 miRNAs, 37 lncRNAs, 256 mRNAs, and 64 circRNAs changed, indicating that they may be involved in the neurotoxic process of aluminum.

In order to deeply understand the functions of DEGs and the main signal transduction pathways and biochemical metabolic pathways involved in their transcription proteins, we performed GO enrichment and KEGG pathway analysis. The GO item includes three parts: biological process, molecular function, and cellular component, which we showed together in this article. The results show that transmembrane transport is the most enriched GO entry. It was reported that low-density lipoprotein receptor-related protein 1 (LRP1) becomes a risk factor for AD by affecting the transmembrane transport of APP.[47] The aluminum ion enters the cell to reduce the accumulation of inositol phosphate, thereby affecting the G protein-coupled transmembrane signal transduction, and can change the membrane-like function of the blood-brain barrier, becoming a definite neurotoxin.[48,49] Our KEGG analysis results showed that the genes on the PI3K/AKT signaling pathway showed significant differences after aluminum treatment. The PI3K/AKT pathway is an important pathway in cell activities, involved in the occurrence and development of tumors, glucose metabolism, and nervous system diseases.[50–52] It is reported that the PI3K/AKT/CREB signaling pathway activity is reduced in AD mice.[53] Workers occupationally exposed to aluminum showed cognitive dysfunction, and their serum PI3K/Akt/mTOR expression was down-regulated.[54]

lncRNA and circRNA have miRNA binding sites and can be used as miRNA sponge to inhibit the negative regulation of miRNA on target genes, thereby indirectly regulating gene expression. This theory becomes the ceRNA mechanism.[55] At the transcriptome level, ceRNA networks of circRNA/lncRNA-miRNA-mRNA were constructed to reveal a new mechanism for ncRNA to regulate gene expression.[56,57] Therefore, we constructed circRNA/lncRNA-miRNA-mRNA networks of all DEGs, DEGs in PI3K-AKT pathway, and IRS1. Our results show that the expression of rno-miR-101b-3p is decreased, and the expression of rno-miR-665 is increased, which are the core molecules in the ceRNA networks of DEGs after aluminum treatment. Sun et al. performed RNA sequencing on the hippocampus of mice exposed to sevoflurane, and the results also showed that miR-101b-3p expression was down-regulated, which may be a molecular target to prevent cognitive impairment caused by sevoflurane.[58] The literature also reported that propofol up-regulated the expression of rno-miR-665, thereby inhibiting BCL2L1 and increasing the expression of caspase-3, resulting in neurotoxicity.[59] In the ceRNA networks of DEGs in PI3K-AKT signaling pathway, the novel circRNA rno_circ_0,001,722 and rno-miR-34c-5p are at the core. There are few studies on miR-34c-5p, and the literature shows that its expression is related to the TNM staging of nasopharyngeal carcinoma.[60]

After insulin binds to the insulin receptor, its tyrosine kinase activity increases, which phosphorylates the tyrosine residues of IRS1 and increases its activity. Mutation or abnormal expression of IRS1 is mainly related to type II diabetes, insulin resistance, cognitive dysfunction and tumor.[61–64] Kapogiannis et al. measured human plasma exosomes, and the results showed that IRS1 (p-Ser312) and its tyrosine phosphorylation in AD group were significantly different from other groups.[65] Decreased expression of IRS1 or decreased tyrosine phosphorylation will reduce the activation of its downstream target PI3K, thereby inhibiting the activity of AKT. Jo EH et al. reported that AKT is involved in glucose metabolism, Aβ deposition and abnormal phosphorylation of tau protein.[66] Our RNA sequencing and PCR-validation results showed that the expression of IRS1 was significantly reduced in the aluminum-exposed group. The results of PPI network of co-expressed DEGs show that IRS1 is at the core position, and it interacts with multiple proteins in structure and function. Horike et al. found that high expression of SIK2 can phosphorylate the Ser794 site of IRS1, leading to insulin resistance.[67] In the results of ceRNA networks of Irs1, rno-miR-143-5p and rno-miR-96-5p are at the center. The researches on Irs1

and miR-143 mostly focused on tumor and sugar metabolism.[68,69] Overexpression of miR-96 inhibits IRS1 leading to insulin resistance and impaired glycogen synthesis.[70] However, there are few studies on IRS1 and miR-143/96, especially in AD or aluminum toxicity studies.

The previous water maze, Nissl staining and TEM proved that we successfully established the aluminum exposure rat model. Next, we verified the reliability of the sequencing results with PCR. IHC and ELISA were used to qualitatively and quantitatively observe the expression of $A\beta_{1-42}$ in the hippocampus of rats. The results showed that aluminum exposure increased the level of $A\beta_{1-42}$ and was positively correlated with the exposure dose. Western blotting was used to detect the protein expression level of the IRS1/PI3K/AKT pathway, and the results showed that the pathway was inhibited, thereby activating the downstream GSK3beta activity, leading to increased expression of $A\beta_{1-42}$ and abnormal phosphorylation of tau protein. In order to verify the authenticity of the ceRNA network, we constructed an AAV intervention rat model. The results showed that inhibiting the expression of miR-96-5p would increase the expression of IRS1 in a targeted manner, thereby activating the PI3K/AKT pathway, improving the learning and memory ability of aluminum-exposed rats, repairing the number of neurons and synaptic structure, and reducing $A\beta_{1-42}$ and tau protein. It demonstrated that miR-96-5p targets and regulates IRS1 and participates in the neurotoxic process of aluminum.

In conclusion, this study enriches the neurotoxicity gene database from the perspective of toxicology, provides a new strategy for studying the neurotoxicity of aluminum, and provides a new strategy for finding biological targets for the prevention and treatment of AD.

MATERIALS AND METHODS

Al-exposed rat model

Fifty-two 8-week-old male Sprague Dawley (SD) rats were obtained from the Experimental Animal Center of Beijing Xingwang (SCXK, 2012-0004), fed in the standard conditions (22 ± 2°C, 45%–55% humidity, noise less than 60 dB and 12-h light/dark cycle) and provided with clean water and standard food *ad libitum*. Rats were randomly divided into four groups (13 rats each): control group, low-dose group (10 μmol/kg $Al(mal)_3$), medium-dose group (20 μmol/kg $Al(mal)_3$), and high-dose group (40 μmol/kg $Al(mal)_3$). After 1 week of adaptive feeding, rats were treated with $Al(mal)_3$ by intraperitoneal (i.p.) injection every other day for 3 months. All animal experiments were approved by the Institutional Animal Care and Use Committee of Shanxi Medical University.

Adeno-associated virus intervention rat model

Sixty 8-week-old male SD rats were kept under the same conditions as the Al-exposed rat model and divided into six groups (10 rats each): control, AAV-control, $Al(mal)_3$, $Al(mal)_3$+AAV-control, $Al(mal)_3$+AAV-miR-96-5p-sponge, and AAV-miR-96-5p-sponge. We constructed the AAV-hSyn-EGFP-miR96-5p-sponge virus (Gene Chem Co., China) to block miR-96-5p in the hippocampus. For viral injection, rats were anesthetized with 10% chloral hydrate (3 mL/kg, i.p.) and fixed in a stereotaxic frame (NARISHIGE, Japan). Holes were drilled at the position coordinating AP: 3.5 mm, ML: 2 mm, and DV: 3 mm in the CA1 area of bilateral hippocampus. The virus injection volume was 3 μL on each side, the titer was 1 vg/mL, and the injection speed was 0.2 μL/min. After the injection, the needle was kept for 5 min and then slowly withdrawn. And then, the rats in the aluminum group were i.p. injected with 20 μmol/kg $Al(mal)_3$ every other day for 3 months.

Morris Water Maze

After the models were constructed, Morris Water Maze (MWM) was performed to assess the learning and memory abilities of all rats. The maze was a circular pool with a height of 60 cm and a diameter of 130 cm. The pool was divided into four quadrants, and the platform was placed in the middle of the NE quadrant, submerged 2 cm below the water surface. The day before the start of the test, each rat was allowed to swim for 120 s to adapt to the environment. During the first 5 days of the formal test, positioning navigation training was conducted. The rats entered the pool in different order from the four directions of S, W, NE, and SE. If the rat found the platform and stayed stable for 10 s, the system stopped timing, which was the escape latency of the rat this time. If the rat did not find the platform within 120 s, it would be manually guided to the platform and stayed for 10 s. The daily escape latency of rats was the average of the four directions on that day. On the sixth day, the space exploration experiment was carried out. We removed the platform and the rats entered the pool from the SW quadrant. The system automatically recorded the number of times the rat crossed the platform and the time it stayed in the NE quadrant within 120 s. A video camera placed above the maze was used to record the swimming path of each rat and Smart v3.0 software was used to analyze the data.

Nissl staining

Nissl staining was used to observe the pathological changes of rat hippocampus. After both models were completed, the rats were infused with normal saline and 4% paraformaldehyde. Brain tissues were taken out and made into paraffin blocks and then cut into 7-μm-thick sections. After routine deparaffinization, the sections were incubated with methyl violet staining solution for 15 min. After rinsing with distilled water, the sections were differentiated with Nissl Differentiation for 5 s. After fully rinsing in xylene, the sections were sealed with neutral resin. OLYMPUS DP72 (OLYMPUS, Japan) was used to observe and take pictures of the sections and ImageJ was used to count the number of neurons in hippocampus CA1 region per 100-μm length.

Transmission electron microscopy

TEM can be used to observe the synaptic structure of neurons in the CA1 region of the rat hippocampus. After the rats were anesthetized and perfused with 4% paraformaldehyde, the brain was quickly removed and the hippocampus tissue was isolated. The hippocampal CA1 area was cut into 1-mm^3 tissue pieces and placed in 2% glutaraldehyde for fixation at 4°C for 2 h. After washing the tissue block four times with buffer solution, it was fixed in 1% OSO4 for

90 min, and then dehydrated by acetone gradient for 15 min each time. The tissue was embedded with epoxy resin 618, and then sliced into 50-nm sections using an ultramicrotome (LKB, Sweden). The sections were stained with uranyl acetate and lead citrate for 30 min, and then they could be observed by TEM (JEM-100CXII, Japan). ImageJ was used to calculate the area and length of the PSD zone to get its average thickness.

RNA extraction, library construction, and sequencing

RNA-seq was performed in six rats: three from the control group and three from the 20 μmol/kg $Al(mal)_3$ group from Al-exposed rat model. Total RNA of the entire hippocampus was extracted by using TRIzol (TaKaRa) according to the instructions. Agarose gel electrophoresis was used to detect RNA degradation and contamination. The RNA purity was measured by using an Eppendorf μCuvette G1.0 (Eppendorf, German), its integrity was assessed by using an Agilent 2100 Bioanalyzer system (Agilent, USA), and its concentration was detected by using a Qubit RNA Assay Kit in a Qubit 2.0 Fluorometer (Life Technologies, USA), which cannot be lower than 400 ng/μL.

After quality inspection, 3 μg RNA of each sample was used to construct cDNA libraries. First, Ribo-Zero rRNA Removal Kit (Epicentre, USA) was used to remove ribosomal RNA (rRNA), and then cDNA libraries were constructed from rRNA-free RNA by using the NEBNext Ultra Directional RNA Library Prep Kit for Illumina (NEB, USA). After the quality was assessed by the Agilent 2100 Bioanalyzer system, cDNA libraries were sequenced on an Illumina HiSeq 2500 platform (Illumina, USA). The library construction and sequencing were undertaken by Novogene Corporation (China) for miRNA, lncRNA, mRNA, and circRNA.

Gene expression level and differential expression analysis

Cufflinks and Cuffdiff were used to quantitatively analyze the transcripts of lncRNA and mRNA, and Find_circ was used to identify circRNA.[71,72] miRBase (http://www.mirbase.org/) was used to identify known miRNAs, and miRDeep2 to predict previously unidentified miRNAs.[73] The expression levels of miRNAs, lncRNA, mRNA, and circRNAs were estimated in terms of TPM values. Edger was used to identify differentially expressed RNAs.[74] All the above software used the default parameters; $p < 0.05$ was defined as differentially expressed transcripts.

GO annotations, KEGG pathway analysis, and PPI network of co-expressed DEGs

GO is a standard glossary term for biological functional annotation.[75] KEGG is a database resource collecting of genomes, biological process, diseases, compounds and so on.[76] Cluster profiler was used for GO annotation and KEGG pathway enrichment analysis.[77] PPI network is helpful to study the molecular mechanism of disease and find new drug targets. String (https://string-db.org/) was used for protein interaction analysis; $p < 0.05$ was considered statistically different.

ceRNA network analysis

We considered all the differentially expressed miRNAs, lncRNAs, ceRNAs, and mRNAs, and drew global ceRNA networks based on the correlation between various analyses. Cytoscape was used to draw the ceRNA networks.[78] The interaction between differential miRNA and circRNA/lncRNA/mRNA whose expression trends were opposite was predicted by targetscan. These interactions were imported into Cytoscape, and the networks were constructed using yfile-radial-layout.

Quantitative real-time PCR validation

RNA sequencing results were verified by RT-PCR. Total RNA was extracted from rat hippocampus using TRIzol (TaKaRa, Japan) according to the instructions, and the purity and concentration of RNA were measured by Eppendorf μCuvette G1.0 (Eppendorf, Germany). Total RNA was reverse transcribed into two kinds of cDNAs, one for PCR of mRNA, lncRNA, and circRNA (RR047, TaKaRa, Japan), and the other for PCR of miRNA (638313, TaKaRa, Japan). RT-PCR was performed using SYBR green mix (RR820,Takara, Japan) in an Applied Biosystems 7500 System (ABI, USA). The 20-μL PCR reaction volume contained 6.4 μL H_2O, 0.8 μL F primer, 0.8 μL R primer, 2 μL cDNA, and 10 μL SYBR green mix, and the PCR reaction conditions were 95°C 10 min, 1 cycle; 95°C 10 s, 60°C 20 s, 72°C 10 s, 40 cycles. The glyceraldehyde-3-phosphate dehydrogenase gene (Gapdh) was used as an endogenous control for mRNA, lncRNA, and circRNA, and U6 was for miRNA. The specific primers were listed in Table 2. The relative RNA expression levels were calculated using the $2^{-\Delta\Delta Ct}$ method.

Immunohistochemistry analysis of $A\beta_{1-42}$

IHC was used to observe the changes in the expression of $A\beta_{1-42}$ protein in the CA1 region of the rat hippocampus. The paraffin blocks of rat brain tissues were cut into 5-μm-thick sections, and baked in a 60℃ oven for 3 h. The sections were deparaffinized through xylene twice for 20 min and rehydrated through descending grades of ethanol (100%, 95%, 85%, 75%) down to water. After 3% hydrogen peroxide was used to remove endogenous oxidase, the sections were then used for antigen retrieval with sodium citrate. After the sections were blocked with serum, they were incubated overnight with $A\beta_{1-42}$ primary antibody ($A\beta_{1-42}$, 1:400, Abcam, ab216504) at 4°C. On the second day, the sections could be mounted after incubation with secondary antibody (KGOS300, KeyGEN, China), DAB coloration, hematoxylin staining, ethanol gradient dehydration, and xylene transparency. The images were captured using OLYMPUS DP72 and the positive area was calculated by ImageJ.

ELISA analysis of $A\beta_{1-42}$

ELISA was performed to measure the levels of $A\beta_{1-42}$ in the rat hippocampus. The hippocampal tissue was homogenized and centrifuged, and the supernatant was taken. The total protein concentration was determined by the BCA protein detection kit (CWBIO, China). The concentration of $A\beta_{1-42}$ in each sample was determined with an ELISA kit (JiangLai, China) according to the manufacturer's instruction. The stock standard was diluted in proportion

Table 2. The specific primers used in RT-PCR

Gene	Primer sequences	
Irs1	F: 5′-AAGCACCTATGCCAGCATCAAC-3′	R: 5′-GAGGATTGCTGAGGTCATTTAGGTC-3′
Gnb3	F: 5′-GACCTGTCGCCAGACTTTCA-3′	R: 5′-CTGCCCTCAGGTCAAAGAGG-3′
Vwf	F: 5′-ACTAGACGTTTCCCTTGCCG-3′	R: 5′-GATGTCCAGGTATGGCTCGG-3′
Itgb6	F: 5′-GCATCCTCTTCCCACACCAA-3′	R: 5′-CCAAGTCCCACAGGCTTGAT-3′
Fn1	F: 5′-GGAGCCTTCACACATCACCA-3′	R: 5′-GTGGCCTGGAATGGTAGCTT-3′
Col6a2	F: 5′-GTGATGGTCCAAAGGGGGAG-3′	R: 5′-CTTGGCTCCTTTACTGCCGA-3′
Sgk1	F: 5′-GCCAGTGCCTTGGGTTATCT-3′	R: 5′-ATGTTCTCCTTGCAGAGCCC-3′
Fgf1	F: 5′-ATGGACACCGAAGGGCTTTT-3′	R: 5′-AAACCAGTTCTTCTCCGCGT-3′
Thbs2	F: 5′-GCTACCAATGCCACCTACCA-3′	R: 5′-AAGCATCTCCGATTCCGTCC-3′
LNC000559	F: 5′-TATCAGTCTCAACCAGTCTAAACCC-3′	R: 5′-TAACAGCTAGGAAGTCGCAACA-3′
LNC000152	F: 5′-TGCCACATCTGGTGCTTGC-3′	R: 5′-GACCGAGGCAACTTGTAAACC-3′
Gapdh	F: 5′-CCATTCTTCCACCTTTGATGCT-3′	R: 5′-TGTTGCTGTAGCCATATTCATTGT-3′
circ_0,005,551	F: 5′-CATTGGCTAAAGAGAGGCAGAA-3′	R: 5′-TCTGGGCTTGCTGTATGTGG-3′
rno-miR-96-5p	F: 5′-GGCACTAGCACATTTTTGCTAAA- 3′	Sequence selected from Taraka 638313 reagent
rno-miR-143-3p	F: 5′-GCAGTGCTGCATCTCTGGAA-3′	Sequence selected from Taraka 638313 reagent
rno-miR-144-3p	F: 5′-CCGCTACAGTATAGATGATGTACTAA-3′	Sequence selected from Taraka 638313 reagent
rno-miR-145-3p	F: 5′-AGTTTTCCCAGGAATCCCTAAA-3′	Sequence selected from Taraka 638313 reagent
rno-miR-183-5p	F: 5′-TATGGCACTGGTAGAATTCACTAAA-3′	Sequence selected from Taraka 638313 reagent
rno-miR-337-3p	F: 5′-TTCAGCTCCTATATGATGCCTTTAA-3′	Sequence selected from Taraka 638313 reagent
U6	F: 5′-GGAACGATACAGAGAAGATTAGC-3′	R: 5′-TGGAACGCTTCACGAATTTGCG-3′

(40–1.25 ng/mL) to establish a standard curve. The optical density was measured at 450 nm using BioTek ELx800 (BioTek, USA).

Western blotting analysis of IRS1/PI3K/AKT pathway

Western blotting was used to detect the expression levels of IRS1/PI3K/AKT signaling pathway proteins in rat hippocampus. The acquisition and concentration determination of total protein in rat hippocampus were the same as the ELISA experiment. The quantified protein sample and the loading buffer were mixed at a ratio of 4:1 and then boiled for 5 min. The protein was separated by SDS-PAGE, and then transferred to polyvinylidene fluoride membrane. After the membranes were blocked with 5% skimmed milk powder for 1 h, they were incubated with the primary antibodies (IRS1, 1:1000, CST, 2382S; AKT 1:1000, CST, 9272S; p-AKT, 1:2000, CST, 4060S; GSK3β, 1:1000, Abcam, ab93926; p-GSK3β, 1:1000, Abcam, ab131097; tau, 1:1000, Abcam, ab32057; p-tau, 1:1000, Abcam, ab109390; β-actin, 1:2000, CWBIO , CW0096) at 4°C overnight. β-actin was used as loading control. After washing, the membranes were incubated with the secondary antibody for 2 h. ECL chemiluminescence solution was used to develop the color of the membranes, and Quantity One software was used to calculate the gray value of protein bands.

Statistical analysis

All data are displayed as mean ± standard deviation (SD). SPSS 22.0 (IBM Corp., Armonk, NY) was used for statistical analysis of the data. Repeated measurement analysis was used for repeated measurement data. One-way ANOVA was used for comparison of results between multiple groups, then least significant difference test was used when the variance was uniform, or the Games-Howell test was used. GraphPad Prism 8 (GraphPad Software, Inc., La Jolla, CA) was performed to draw graphs of statistical results; $p < 0.05$ was considered statistically significant.

SUPPLEMENTAL INFORMATION

Supplemental information can be found online at https://doi.org/10.1016/j.omtn.2021.11.010.

ACKNOWLEDGMENTS

This research was financially supported by the National Natural Science Foundation of China (No. 81872599). We sincerely thank colleagues for their help and work on the research.

AUTHOR CONTRIBUTIONS

C.H., X.Z., Y.L., J.N., and X.L. contributed to animal experiments and data analysis. J.S., L.W., H.L., F.L., and Y.Z. performed the molecular experiments and analyzed the data. C.H. and Q.N. designed the study and wrote the manuscript. All authors read and approved the final manuscript.

DECLARATION OF INTERESTS

The authors declare that there are no conflicts of interest.

REFERENCES

1. Dabeka, R., Fouquet, A., Belisle, S., and Turcotte, S. (2011). Lead, cadmium and aluminum in Canadian infant formulae, oral electrolytes and glucose solutions. Food Addit Contam. Chem. Anal Control Expo. Risk Assess. *28*, 744–753.
2. Exley, C. (2013). Human exposure to aluminium. Environ. Sci. Process. Impacts *15*, 1807–1816.
3. Priest, N.D. (2004). The biological behaviour and bioavailability of aluminium in man, with special reference to studies employing aluminium-26 as a tracer: review and study update. J. Environ. Monit. JEM *6*, 375–403.
4. Savory, J., Herman, M.M., and Ghribi, O. (2006). Mechanisms of aluminum-induced neurodegeneration in animals: implications for Alzheimer's disease. J. Alzheimer's Dis. JAD *10*, 135–144.
5. Rondeau, V., Jacqmin-Gadda, H., Commenges, D., Helmer, C., and Dartigues, J.F. (2009). Aluminum and silica in drinking water and the risk of Alzheimer's disease or cognitive decline: findings from 15-year follow-up of the PAQUID cohort. Am. J. Epidemiol. *169*, 489–496.
6. Song, J., Liu, Y., Zhang, H.F., and Niu, Q. (2016). The RAS/PI3K pathway is involved in the impairment of long-term potentiation induced by acute aluminum treatment in rats. Biomed. Environ. Sci. BES *29*, 782–789.
7. Li, H., Xue, X., Li, Z., Pan, B., Hao, Y., and Niu, Q. (2020). Aluminium-induced synaptic plasticity injury via the PHF8-H3K9me2-BDNF signalling pathway. Chemosphere *244*, 125445.
8. Riihimäki, V., Hänninen, H., Akila, R., Kovala, T., Kuosma, E., Paakkulainen, H., et al. (2000). Body burden of aluminum in relation to central nervous system function among metal inert-gas welders. Scand. J. Work Environ. Health *26*, 118–130.
9. Pohanka, M. (2014). Copper, aluminum, iron and calcium inhibit human acetylcholinesterase in vitro. Environ. Toxicol. Pharmacol. *37*, 455–459.
10. Wang, H., Shao, B., Yu, H., Xu, F., Wang, P., Yu, K., et al. (2019). Neuroprotective role of hyperforin on aluminum maltolate-induced oxidative damage and apoptosis in PC12 cells and SH-SY5Y cells. Chem. Biol. Interact *299*, 15–26.
11. Toimela, T., and Tähti, H. (2004). Mitochondrial viability and apoptosis induced by aluminum, mercuric mercury and methylmercury in cell lines of neural origin. Arch. Toxicol. *78*, 565–574.
12. Rodella, L.F., Ricci, F., Borsani, E., Stacchiotti, A., Foglio, E., Favero, G., et al. (2008). Aluminium exposure induces Alzheimer's disease-like histopathological alterations in mouse brain. Histol. Histopathol *23*, 433–439.
13. Oshima, E., Ishihara, T., Yokota, O., Nakashima-Yasuda, H., Nagao, S., Ikeda, C., et al. (2013). Accelerated tau aggregation, apoptosis and neurological dysfunction caused by chronic oral administration of aluminum in a mouse model of tauopathies. Brain Pathol. (Zurich, Switzerland) *23*, 633–644.
14. Qin, X., Li, L., Nie, X., and Niu, Q. (2020). Effects of chronic aluminum lactate exposure on neuronal apoptosis and hippocampal synaptic plasticity in rats. Biol. Trace Elem. Res. *197*, 571–579.
15. Peng, Z., Cheng, Y., Tan, B.C., Kang, L., Tian, Z., Zhu, Y., et al. (2012). Comprehensive analysis of RNA-Seq data reveals extensive RNA editing in a human transcriptome. Nat. Biotechnol *30*, 253–260.
16. Yan, T., Cui, H., Zhou, Y., Yang, B., Kong, P., Zhang, Y., et al. (2019). Multi-region sequencing unveils novel actionable targets and spatial heterogeneity in esophageal squamous cell carcinoma. Nat. Commun *10*, 1670.
17. Langlais, D., Fodil, N., and Gros, P. (2017). Genetics of infectious and inflammatory diseases: overlapping discoveries from association and exome-sequencing studies. Annu. Rev. Immunol. *35*, 1–30.
18. Konrad, E.D.H., Nardini, N., Caliebe, A., Nagel, I., Young, D., Horvath, G., et al. (2019). CTCF variants in 39 individuals with a variable neurodevelopmental disorder broaden the mutational and clinical spectrum. Genet. Med. Off J. Am. Coll. Med. Genet. *21*, 2723–2733.
19. Chen, L., Zhu, B., Guo, Y., Xu, T., Lee, J.S., Qian, P.Y., et al. (2016). High-throughput transcriptome sequencing reveals the combined effects of key e-waste contaminants, decabromodiphenyl ether (BDE-209) and lead, in zebrafish larvae. Environ. Pollut. *214*, 324–333.
20. Li, S., Shi, M., Wan, Y., Wang, Y., Zhu, M., Wang, B., et al. (2020). Inflammasome/NF-κB translocation inhibition via PPARγ agonist mitigates inorganic mercury induced nephrotoxicity. Ecotoxicol Environ. Saf. *201*, 110801.
21. Kwok, M.L., Meng, Q., Hu, X.L., Chung, C.T., and Chan, K.M. (2020). Whole-transcriptome sequencing (RNA-seq) study of the ZFL zebrafish liver cell line after acute exposure to Cd(2+) ions. Aquat. Toxicol. (Amsterdam, Netherlands) *228*, 105628.
22. Fabian, M.R., Sonenberg, N., and Filipowicz, W. (2010). Regulation of mRNA translation and stability by microRNAs. Annu. Rev. Biochem. *79*, 351–379.
23. Salmena, L., Poliseno, L., Tay, Y., Kats, L., and Pandolfi, P.P. (2011). A ceRNA hypothesis: the Rosetta Stone of a hidden RNA language? Cell *146*, 353–358.
24. Fan, C.N., Ma, L., and Liu, N. (2018). Systematic analysis of lncRNA-miRNA-mRNA competing endogenous RNA network identifies four-lncRNA signature as a prognostic biomarker for breast cancer. J. Transl Med. *16*, 264.
25. Xiong, D.D., Dang, Y.W., Lin, P., Wen, D.Y., He, R.Q., Luo, D.Z., et al. (2018). A circRNA-miRNA-mRNA network identification for exploring underlying pathogenesis and therapy strategy of hepatocellular carcinoma. J. Transl Med. *16*, 220.
26. Mercado-Gómez, O., Hernández-Fonseca, K., Villavicencio-Queijeiro, A., Massieu, L., Chimal-Monroy, J., and Arias, C. (2008). Inhibition of Wnt and PI3K signaling modulates GSK-3beta activity and induces morphological changes in cortical neurons: role of tau phosphorylation. Neurochem. Res. *33*, 1599–1609.
27. Denver, P., English, A., and McClean, P.L. (2018). Inflammation, insulin signaling and cognitive function in aged APP/PS1 mice. Brain Behav. Immun. *70*, 423–434.
28. Ma, N., Liu, Z.P., Yang, D.J., Liang, J., Zhu, J.H., Xu, H.B., et al. (2016). Risk assessment of dietary exposure to aluminium in the Chinese population. Food Addit Contam. Chem. Anal Control Expo. Risk Assess. *33*, 1557–1562.
29. Exley, C., and Mold, M.J. (2015). The binding, transport and fate of aluminium in biological cells. J. Trace Elem. Med. Biol. Organ Soc. Miner Trace Elem. (Gms) *30*, 90–95.
30. Crapper, D.R., Krishnan, S.S., and Dalton, A.J. (1973). Brain aluminum distribution in Alzheimer's disease and experimental neurofibrillary degeneration. Science *180*, 511–513.
31. Tomljenovic, L. (2011). Aluminum and Alzheimer's disease: after a century of controversy, is there a plausible link? J. Alzheimer's Dis. JAD *23*, 567–598.
32. Giorgianni, C., Faranda, M., Brecciaroli, R., Beninato, G., Saffioti, G., Muraca, G., et al. (2003). Cognitive disorders among welders exposed to aluminum. G Ital. Med. Del. Lav Ergon. *25*, 102–103.
33. House, E., Collingwood, J., Khan, A., Korchazkina, O., Berthon, G., and Exley, C. (2004). Aluminium, iron, zinc and copper influence the in vitro formation of amyloid fibrils of Abeta42 in a manner which may have consequences for metal chelation therapy in Alzheimer's disease. J. Alzheimer's Dis. JAD *6*, 291–301.
34. Zhao, H.H., Di, J., Liu, W.S., Liu, H.L., Lai, H., and Lü, Y.L. (2013). Involvement of GSK3 and PP2A in ginsenoside Rb1's attenuation of aluminum-induced tau hyperphosphorylation. Behav. Brain Res. *241*, 228–234.
35. Pan, B., Li, Y., Zhang, J., Zhou, Y., Li, L., Xue, X., et al. (2020). Role of mGluR 1 in synaptic plasticity impairment induced by maltol aluminium in rats. Environ. Toxicol. Pharmacol. *78*, 103406.
36. He, C., Zhao, X., Li, H., Wang, F., Zhang, J., Wang, Y., et al. (2021). Regulation of mGluR1 on the expression of PKC and NMDAR in aluminum-exposed PC12 cells. Neurotox Res. *39*, 634–644.
37. Lee, K.G., and Shibamoto, T. (2000). Antioxidant properties of aroma compounds isolated from soybeans and mung beans. J. Agric. Food Chem. *48*, 4290–4293.
38. Guo, N., Li, C., Liu, Q., Liu, S., Huan, Y., Wang, X., et al. (2018). Maltol, a food flavor enhancer, attenuates diabetic peripheral neuropathy in streptozotocin-induced diabetic rats. Food Funct. *9*, 6287–6297.
39. Khoury, A., Pagan, K.A., and Farland, M.Z. (2021). Ferric maltol: a new oral iron formulation for the treatment of iron deficiency in adults. Ann. Pharmacother. *55*, 222–229.
40. Kaneko, N., Yasui, H., Takada, J., Suzuki, K., and Sakurai, H. (2004). Orally administrated aluminum-maltolate complex enhances oxidative stress in the organs of mice. J. Inorg. Biochem. *98*, 2022–2031.
41. Vorhees, C.V., and Williams, M.T. (2006). Morris water maze: procedures for assessing spatial and related forms of learning and memory. Nat. Protoc. *1*, 848–858.

42. Zhu, W., Wang, X.R., Du, S.Q., Yan, C.Q., Yang, N.N., Lin, L.L., et al. (2018). Antioxidative and anti-apoptotic effects of acupuncture: role of thioredoxin-1 in the hippocampus of vascular dementia rats. Neuroscience *379*, 281–291.

43. Stark, R., Grzelak, M., and Hadfield, J. (2019). RNA sequencing: the teenage years. Nat. Rev. Genet. *20*, 631–656.

44. Li, Y.C., Shen, J.D., Lu, S.F., Zhu, L.L., Wang, B.Y., Bai, M., et al. (2020). Transcriptomic analysis reveals the mechanism of sulfasalazine-induced liver injury in mice. Toxicol. Lett. *321*, 12–20.

45. Chen, Q.Y., Shen, S., Sun, H., Wu, F., Kluz, T., Kibriya, M.G., et al. (2020). PBMC gene expression profiles of female Bangladeshi adults chronically exposed to arsenic-contaminated drinking water. Environ. Pollut. *259*, 113672.

46. Nan, A., Chen, L., Zhang, N., Liu, Z., Yang, T., Wang, Z., et al. (2017). A novel regulatory network among LncRpa, CircRar1, MiR-671 and apoptotic genes promotes lead-induced neuronal cell apoptosis. Arch. Toxicol. *91*, 1671–1684.

47. Eggert, S., Thomas, C., Kins, S., and Hermey, G. (2018). Trafficking in Alzheimer's disease: Modulation of APP transport and processing by the transmembrane proteins LRP1, SorLA, SorCS1c, Sortilin, and Calsyntenin. Mol. Neurobiol. *55*, 5809–5829.

48. Haug, A., Shi, B., and Vitorello, V. (1994). Aluminum interaction with phosphoinositide-associated signal transduction. Arch. Toxicol. *68*, 1–7.

49. Banks, W.A., and Kastin, A.J. (1989). Aluminum-induced neurotoxicity: alterations in membrane function at the blood-brain barrier. Neurosci. Biobehav Rev. *13*, 47–53.

50. Alzahrani, A.S. (2019). PI3K/Akt/mTOR inhibitors in cancer: at the bench and bedside. Semin. Cancer Biol. *59*, 125–132.

51. Shum, M., Bellmann, K., St-Pierre, P., and Marette, A. (2016). Pharmacological inhibition of S6K1 increases glucose metabolism and Akt signalling in vitro and in diet-induced obese mice. Diabetologia *59*, 592–603.

52. Borrie, S.C., Brems, H., Legius, E., and Bagni, C. (2017). Cognitive dysfunctions in intellectual disabilities: the contributions of the Ras-MAPK and PI3K-AKT-mTOR Pathways. Annu. Rev. Genom Hum. Genet. *18*, 115–142.

53. Xia, L., Zhu, X., Zhao, Y., Yang, G., Zuo, X., Xie, P., et al. (2019). Genome-wide RNA sequencing analysis reveals that IGF-2 attenuates memory decline, oxidative stress and amyloid plaques in an Alzheimer's disease mouse model (AD) by activating the PI3K/AKT/CREB signaling pathway. Int. Psychogeriatr, 1–13.

54. Shang, N., Zhang, P., Wang, S., Chen, J., Fan, R., Chen, J., et al. (2020). Aluminum-induced cognitive impairment and PI3K/Akt/mTOR signaling pathway involvement in occupational aluminum workers. Neurotox Res. *38*, 344–358.

55. Smillie, C.L., Sirey, T., and Ponting, C.P. (2018). Complexities of post-transcriptional regulation and the modeling of ceRNA crosstalk. Crit. Rev. Biochem. Mol. Biol. *53*, 231–245.

56. Jin, X., Feng, C.Y., Xiang, Z., Chen, Y.P., and Li, Y.M. (2016). CircRNA expression pattern and circRNA-miRNA-mRNA network in the pathogenesis of nonalcoholic steatohepatitis. Oncotarget *7*, 66455–66467.

57. Ma, N., Tie, C., Yu, B., Zhang, W., and Wan, J. (2020). Identifying lncRNA-miRNA-mRNA networks to investigate Alzheimer's disease pathogenesis and therapy strategy. Aging *12*, 2897–2920.

58. Sun, H., Hu, H., Xu, X., Tao, T., and Liang, Z. (2020). Key miRNAs associated with memory and learning disorder upon exposure to sevoflurane determined by RNA sequencing. Mol. Med. Rep. *22*, 1567–1575.

59. Sun, W.C., Liang, Z.D., and Pei, L. (2015). Propofol-induced rno-miR-665 targets BCL2L1 and influences apoptosis in rodent developing hippocampal astrocytes. Neurotoxicology *51*, 87–95.

60. Wang, F., Lu, J., Peng, X., Wang, J., Liu, X., Chen, X., et al. (2016). Integrated analysis of microRNA regulatory network in nasopharyngeal carcinoma with deep sequencing. J. Exp. Clin. Cancer Res. CR *35*, 17.

61. Mahmutovic, L., Bego, T., Sterner, M., Gremsperger, G., Ahlqvist, E., Velija Asimi, Z., et al. (2019). Association of IRS1 genetic variants with glucose control and insulin resistance in type 2 diabetic patients from Bosnia and Herzegovina. Drug Metab. Personalized Ther. *34*. https://doi.org/10.1515/dmpt-2018-0031.

62. Chen, Z., Yu, H., Shi, X., Warren, C.R., Lotta, L.A., Friesen, M., et al. (2020). Functional screening of candidate causal genes for insulin resistance in human preadipocytes and adipocytes. Circ. Res. *126*, 330–346.

63. Tanokashira, D., Fukuokaya, W., and Taguchi, A. (2019). Involvement of insulin receptor substrates in cognitive impairment and Alzheimer's disease. Neural Regen. Res. *14*, 1330–1334.

64. Lai, Y.Y., Shen, F., Cai, W.S., Chen, J.W., Feng, J.H., Cao, J., et al. (2016). MiR-384 regulated IRS1 expression and suppressed cell proliferation of human hepatocellular carcinoma. Tumour Biol. J. Int. Soc. Oncodevelopmental Biol. Med. *37*, 14165–14171.

65. Kapogiannis, D., Boxer, A., Schwartz, J.B., Abner, E.L., Biragyn, A., Masharani, U., et al. (2015). Dysfunctionally phosphorylated type 1 insulin receptor substrate in neural-derived blood exosomes of preclinical Alzheimer's disease. FASEB J. Off Publ. Fed. Am. Soc. Exp. Biol. *29*, 589–596.

66. Jo, E.H., Ahn, J.S., Mo, J.S., Yoon, J.H., Ann, E.J., Baek, H.J., et al. (2015). Akt1 phosphorylates Nicastrin to regulate its protein stability and activity. J. Neurochem. *134*, 799–810.

67. Horike, N., Takemori, H., Katoh, Y., Doi, J., Min, L., Asano, T., et al. (2003). Adipose-specific expression, phosphorylation of Ser794 in insulin receptor substrate-1, and activation in diabetic animals of salt-inducible kinase-2. J. Biol. Chem. *278*, 18440–18447.

68. Chen, J., Yu, Y., Li, H., Hu, Q., Chen, X., He, Y., et al. (2019). Long non-coding RNA PVT1 promotes tumor progression by regulating the miR-143/HK2 axis in gallbladder cancer. Mol. Cancer *18*, 33.

69. Riches, K., Alshanwani, A.R., Warburton, P., O'Regan, D.J., Ball, S.G., Wood, I.C., et al. (2014). Elevated expression levels of miR-143/5 in saphenous vein smooth muscle cells from patients with Type 2 diabetes drive persistent changes in phenotype and function. J. Mol. Cell Cardiol *74*, 240–250.

70. Yang, W.M., Min, K.H., and Lee, W. (2016). Induction of miR-96 by dietary saturated fatty acids exacerbates hepatic insulin resistance through the suppression of INSR and IRS-1. PloS one *11*, e0169039.

71. Trapnell, C., Hendrickson, D.G., Sauvageau, M., Goff, L., Rinn, J.L., and Pachter, L. (2013). Differential analysis of gene regulation at transcript resolution with RNA-seq. Nat. Biotechnol. *31*, 46–53.

72. Hansen, T.B., Venø, M.T., Damgaard, C.K., and Kjems, J. (2016). Comparison of circular RNA prediction tools. Nucleic Acids Res. *44*, e58.

73. Friedländer, M.R., Mackowiak, S.D., Li, N., Chen, W., and Rajewsky, N. (2012). miRDeep2 accurately identifies known and hundreds of novel microRNA genes in seven animal clades. Nucleic Acids Res. *40*, 37–52.

74. Robinson, M.D., McCarthy, D.J., and Smyth, G.K. (2010). edgeR: a Bioconductor package for differential expression analysis of digital gene expression data. Bioinformatics (Oxford, England) *26*, 139–140.

75. (2019). The gene ontology resource: 20 years and still GOing strong. Nucleic Acids Res. *47*, D330–d338.

76. Kanehisa, M., and Goto, S. (2000). KEGG: kyoto encyclopedia of genes and genomes. Nucleic Acids Res. *28*, 27–30.

77. Zhang, M., Zhu, K., Pu, H., Wang, Z., Zhao, H., Zhang, J., et al. (2019). An immune-related signature predicts survival in patients with lung adenocarcinoma. Front Oncol. *9*, 1314.

78. Shannon, P., Markiel, A., Ozier, O., Baliga, N.S., Wang, J.T., Ramage, D., et al. (2003). Cytoscape: a software environment for integrated models of biomolecular interaction networks. Genome Res. *13*, 2498–2504.